Small

NANO · MICRO small
www.small-journal.com

RESEARCH ARTICLE

Ultrasound-Excited Injectable Piezoelectric Composite Hydrogels for Enhancing Diabetic Flap Survival via Synergistic Redox Homeostasis and Angiogenesis

Mingcheng Tang[1,2,3,4] | Ruizeng Luo[2] | Kun Fang[5] | Yunfan Tang[1] | Yong Chen[1,4] | Qiao Yu[4] | Puqing Yao[6] | Baokun Zhang[4] | Zhou Li[2,3] | Jiaping Zhang[1]

[1]Department of Plastic Surgery, State Key Laboratory of Trauma and Chemical Poisoning, Southwest Hospital, Third Military Medical University (Army Medical University), Chongqing, China | [2]Vita Tech Innovation Center, School of Clinical Medicine, Tsinghua Changgung Hospital, Tsinghua University, Beijing, China | [3]School of Biomedical Engineering, Tsinghua Medicine, Tsinghua University, Beijing, China | [4]Beijing Institute of Nanoenergy and Nanosystems, Chinese Academy of Sciences, Beijing, China | [5]Department of Stomatology, The First Medical Center, Chinese PLA General Hospital, Beijing, China | [6]Beijing Advanced Innovation Center for Biomedical Engineering, School of Biological Science and Medical Engineering, Key Laboratory for Biomechanics and Mechanobiology of Ministry of Education, School of Engineering Medicine, Beihang University, Beijing, China

Correspondence: Zhou Li (li_zhou@tsinghua.edu.cn) | Jiaping Zhang (japzhang@tmmu.edu.cn)

Received: 8 March 2026 | **Revised:** 25 April 2026 | **Accepted:** 29 April 2026

Keywords: angiogenesis | antioxidation | diabetic flaps | piezoelectric stimulation

ABSTRACT

The low survival of skin flap transplantation in diabetic patients is a serious challenge for clinical plastic surgery. The root cause lies in the vicious cycle formed by metabolic disorders caused by persistent hyperglycemia, leading to excessive accumulation of Hydrogen peroxide (H_2O_2), oxidative stress-mediated inflammation, and impaired angiogenesis. This study develops an ultrasound (US)-excited injectable piezoelectric composite hydrogel (iPCH) composed of piezoelectric poly-L-lactic acid (PLLA) short fibers, ferroferric oxide (Fe_3O_4) nanozymes, and a crosslinked gelatin matrix. The PLLA short fibers in the US-excited iPCH can generate piezoelectric stimulation under US-excited conditions, enhancing endothelial cell proliferation, migration, and pro-angiogenic potential. Furthermore, the generated piezoelectric charge accelerates electron transfer on the surface of Fe_3O_4 nanozymes through the piezoelectric effect, significantly enhancing their efficiency in scavenging H_2O_2 and alleviating the local inflammatory response. This improves the long-standing inflammatory microenvironment of diabetic wounds, increasing the survival of endothelial cells under oxidative stress. *In vivo* studies show that the US-excited iPCH can reduce oxidative stress-mediated inflammatory responses, accelerate flap angiogenesis, and ultimately improve flap survival. This study utilizes the synergistic effect of physical stimulation and microenvironment regulation to provide a simple and efficient clinical intervention strategy for the survival of complex flaps.

1 | Introduction

Diabetic ulcers are a common and serious complication of diabetes, affecting over 100 million diabetic patients globally [1, 2]. For extensive chronic lesions with impaired blood perfusion caused by diabetic foot ulcers, flap transplantation is the preferred surgical procedure for the repair of such complex wounds, as it can achieve effective coverage of the defective region and establish a favorable soft tissue structure. However, the hyperglycemic environment in diabetic ulcer patients leads to the accumulation of reactive oxygen species (ROS), mainly hydrogen peroxide (H_2O_2) [3], which further triggers the overexpression of inflammatory cytokines, including tumor necrosis factor-α (TNF-α), interleukin-6 (IL-6), and interleukin-1β (IL-1β). This sustains the inflammatory microenvironment and causes widespread damage to vascular endothelial cells [4–6]. In this environment, the transplanted flap struggles to form a new vascular network with the micro-vessels in the subcutaneous fat, causing local circulatory insufficiency and persistent hypoxia in the transplanted flap, ultimately leading to flap necrosis [7–10].

ROS scavenging is considered an effective way to promote diabetic wound healing [11–13]. It could contribute to attenuating inflammation, relieving cellular and tissue damage, and establishing a favorable microenvironment for enhanced tissue repair [13, 14]. As an effective intervention, antioxidants can alleviate oxidative stress and tissue inflammation, mainly including antioxidant drugs such as α-lipoic acid, metformin, and statins; natural antioxidant enzymes such as superoxide dismutase and catalase; as well as nanozymes with natural antioxidant enzyme-like activities [15, 16]. However, merely alleviating local inflammation cannot promote angiogenesis to establish an active and long-term blood supply, thus failing to fundamentally solve the problem of nutrition and oxygen supply after skin flap transplantation.

Currently, clinical methods for promoting angiogenesis include stem cell therapy, growth factor delivery therapy, and physical stimulation [17]. Electrical stimulation (ES) therapy, as a low-cost, controllable, and safe physical stimulation method, has been proven to significantly promote angiogenesis by promoting cell proliferation and migration, as well as modulating the production of angiogenic factors [18–21]. Based on these understandings, we developed an ultrasound (US)-excited injectable piezoelectric composite hydrogel (iPCH) containing composite short fibers co-spun from ferroferric oxide (Fe_3O_4) nanozymes and poly-L-lactic acid (PLLA) (Figure 1). The Fe_3O_4 nanozymes, possessing catalase activity [22, 23], catalyze excess H_2O_2 in diabetic wounds, mitigating oxidative stress along with oxygen generation, and creating a favorable microenvironment for angiogenesis. As a biocompatible and biodegradable piezoelectric material, PLLA could generate piezoelectric stimulation and promote angiogenesis under US excitation [24, 25]. With an injectable crosslinked gelatin hydrogel as a matrix, the PLLA/ Fe_3O_4 short fibers were delivered and encapsulated beneath the flap. Under US excitation, the US-excited iPCH facilitated flap revascularization by promoting the survival, proliferation, and migration of vascular endothelial cells. This strategy provides a simple and feasible strategy for achieving survival of complex flaps in clinical practice.

2 | Results and Discussion

2.1 | Preparation and Characterization of the US-Excited iPCH

The US-excited iPCH is composed of piezoelectric PLLA/Fe_3O_4 short fibers and a crosslinked gelatin matrix, which has excellent biocompatibility [22, 25, 26]. PLLA is a biodegradable organic piezoelectric material [27–29], providing an ideal material candidate for effectively promoting angiogenesis under US excitation [30, 31]. Fe_3O_4 nanozymes overcome the insufficient activity of natural enzymes in the diabetic microenvironment (pH 7.0–8.9) and exhibit catalase-like activity under neutral and weakly alkaline conditions [32–34]. They can efficiently decompose H_2O_2 into oxygen and water, thereby alleviating oxidative stress in diabetic flaps. PLLA/Fe_3O_4 short fibers were delivered to the underside of the flap via a biodegradable cross-linked gelatin as a hydrogel matrix [35].

Fe_3O_4 nanozymes synthesized via a hydrothermal method were co-spun with PLLA using electrospinning to prepare films. The annealed PLLA/Fe_3O_4 nanofiber films were cut into PLLA/Fe_3O_4 short fibers. The average diameter of the Fe_3O_4 nanozymes was approximately 90 nm (Figure 2a; Figure S1). Scanning electron microscopy (SEM) images of the PLLA/Fe_3O_4 short fibers showed that the surface of the PLLA short fibers exhibited distinct granular protrusions, the same size as the Fe_3O_4 nanozymes (Figure 2a). Elemental analysis of the PLLA/Fe_3O_4 short fibers using energy dispersive spectroscopy (EDS) revealed the presence of Fe in addition to C and O elements found in PLLA, confirming that Fe_3O_4 had been incorporated into PLLA (Figure S2). Fourier transform infrared spectroscopy (FT-IR) analysis further verified the successful preparation and component compatibility of the PLLA/Fe_3O_4 short fibers (Figure 2b). Due to the stretching vibration of Fe-O bonds, the Fe_3O_4 nanozymes showed a characteristic absorption band at ~585 cm^{-1} [36], which was visible in the spectrum of the PLLA/Fe_3O_4 short fibers. Meanwhile, the FT-IR spectra of PLLA/Fe_3O_4 short fibers showed characteristic peaks for the stretching vibrations of the carbonyl group (C═O) (~1750 cm^{-1}) and the ether group (C─O─C) (~1500–1000 cm^{-1}), which are consistent with the characteristic peaks of PLLA. X-ray diffraction (XRD) analysis confirmed the structural stability of the PLLA/Fe_3O_4 short fibers at the crystal structure level (Figure 2c). In the XRD spectrum, characteristic diffraction peaks of Fe_3O_4 nanozymes appeared at 30.1°, 35.5°, 43.2°, 53.6°, 57.3°, and 62.8°, corresponding to the (220), (311), (400), (422), (511), and (440) crystal planes of its crystal, which were consistent with the standard diffraction patterns of Fe_3O_4 (PDF#72-2303), showing that Fe_3O_4 nanozymes had been successfully incorporated into the system and the crystal structure had not changed.

The most direct influences on the piezoelectricity of PLLA are its β-form crystal structure and crystallinity [31]. Annealing, as a method to improve the piezoelectricity of PLLA, can promote the crystallization of oriented PLLA polymer chains and stabilize the β phase structure [37, 38]. The annealed PLLA/Fe_3O_4 nanofiber film exhibited diffraction peaks generated by the (200) and (110) crystal planes, which were in the same positions as the diffraction peaks of annealed PLLA with a β-phase structure (Figure 2c). We calculated the crystallinity of the samples by analyzing the diffraction peaks in their XRD patterns. The crystallinity of annealed PLLA/Fe_3O_4 (~79.5%) was lower than that of annealed PLLA (~92.2%), which might lead to a lower piezoelectricity of annealed PLLA/Fe_3O_4. Therefore, we tested the output performance of annealed PLLA/Fe_3O_4 nanofiber films with different Fe_3O_4 nanozyme contents (0, 5, 10 wt.%) to ensure its piezoelectric effect. The voltage-time curves showed that the pure annealed PLLA exhibited the optimal output performance of piezoelectricity (approximately 1.3 V). As the Fe_3O_4 nanozymes ratio increased from 5% to 10%, the piezoelectric output of the annealed PLLA/Fe_3O_4 nanofiber membranes gradually decreased (~1 and ~0.7 V, respectively) (Figure 2d). This might be related to the

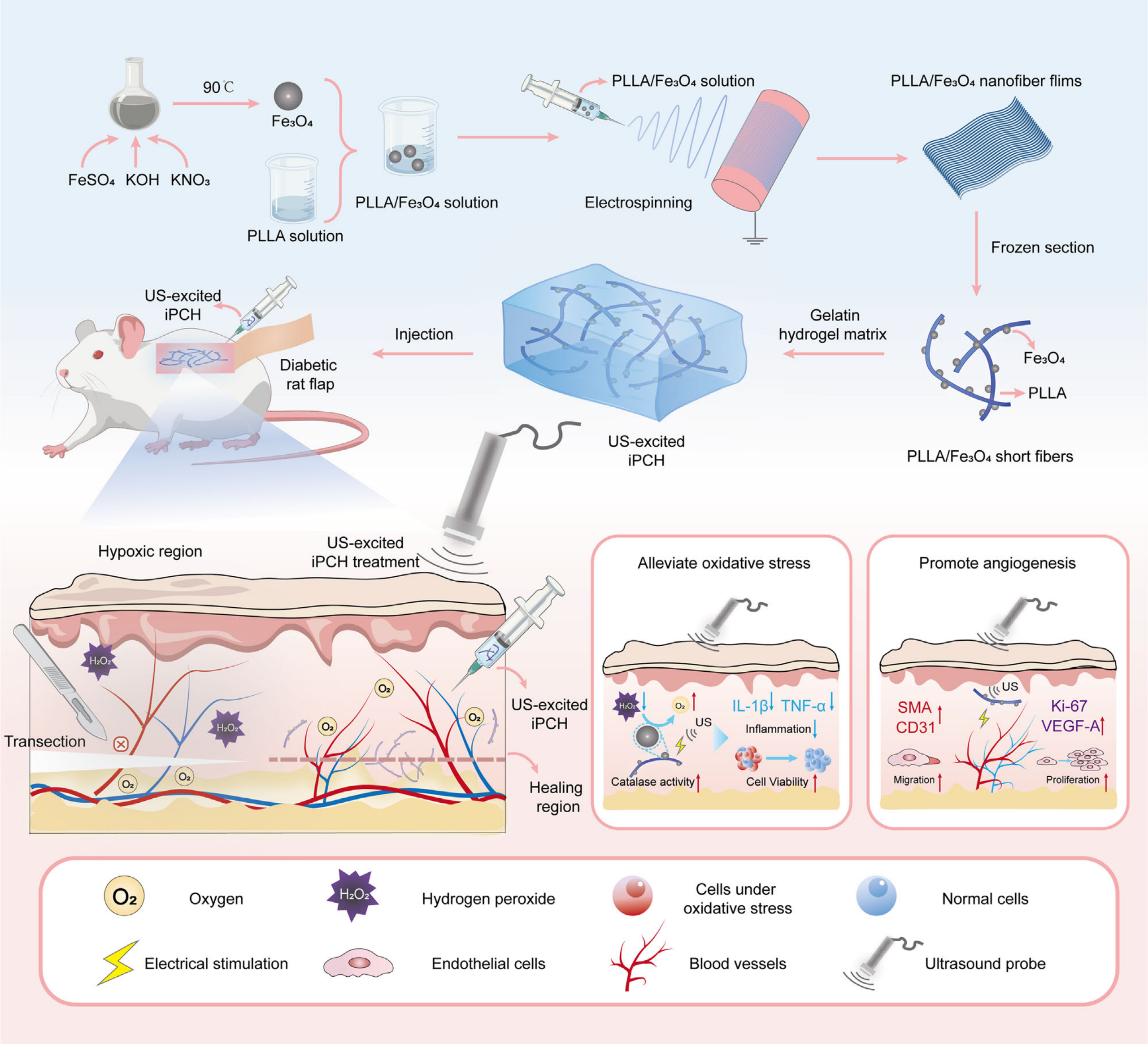

FIGURE 1 | Schematic illustration of the US-excited iPCH improving diabetic flap survival: PLLA/Fe_3O_4 nanofiber films were fabricated via electrospinning, using a mixture of PLLA and hydrothermally synthesized Fe_3O_4 nanozymes. The PLLA/Fe_3O_4 short fibers were obtained by cutting the PLLA/Fe_3O_4 nanofiber films and were subsequently mixed with crosslinked gelatin hydrogel to prepare the US-excited iPCH. Excited by US, the iPCH exhibited piezoelectric stimulation and enhanced Fe_3O_4 catalase activity, ultimately promoting the survival of diabetic rat flaps.

reduction in crystallinity of the crystal structure due to the introduction of the Fe_3O_4 nanozymes.

Since the Fe_3O_4 nanozymes are encapsulated by PLLA, their catalase-like activity needs to be ensured. The PLLA/Fe_3O_4 nanofiber film was cut into 10 µm short fibers using a cryostat (Figure S3), and the enzyme activity was confirmed by detecting the amount of oxygen produced from H_2O_2 catalyzed by PLLA/Fe_3O_4 short fibers with different Fe_3O_4 nanozyme contents. The results showed that short fibers containing 5 and 10 wt.% Fe_3O_4 nanozymes could catalyze H_2O_2 and produce a large amount of O_2, exhibiting the same concentration-dependent catalytic properties as Fe_3O_4 nanozymes (Figure S4). Considering that PLLA/Fe_3O_4 short fibers needed to possess both piezoelectric stimulation and catalase-like activity, PLLA/Fe_3O_4 short fibers loaded with 5 wt.% Fe_3O_4 nanozymes were ultimately selected for further validation.

PLLA/Fe_3O_4 short fibers exhibited a Michaelis constant (K_m) of 204.5 mM in a simulated weakly alkaline environment of diabetic tissue (pH 7.4) (Figure 2e). Moreover, piezoelectric stimulation was found to enhance the catalase activity of Fe_3O_4 nanozymes. Under US excitation, the dissolved oxygen production of the PLLA/Fe_3O_4 short fibers group increased continuously with the extension of reaction time, and its catalytic efficiency was 1.76 times higher than the PLLA/Fe_3O_4 short fibers group without US excitation (Figure 2f); while single US excitation (US group), PLLA short fiber (PLLA group), and piezoelectric stimulation (PLLA + US group) did not show any catalytic performance for H_2O_2. This enhancement might be attributed to the piezoelectric

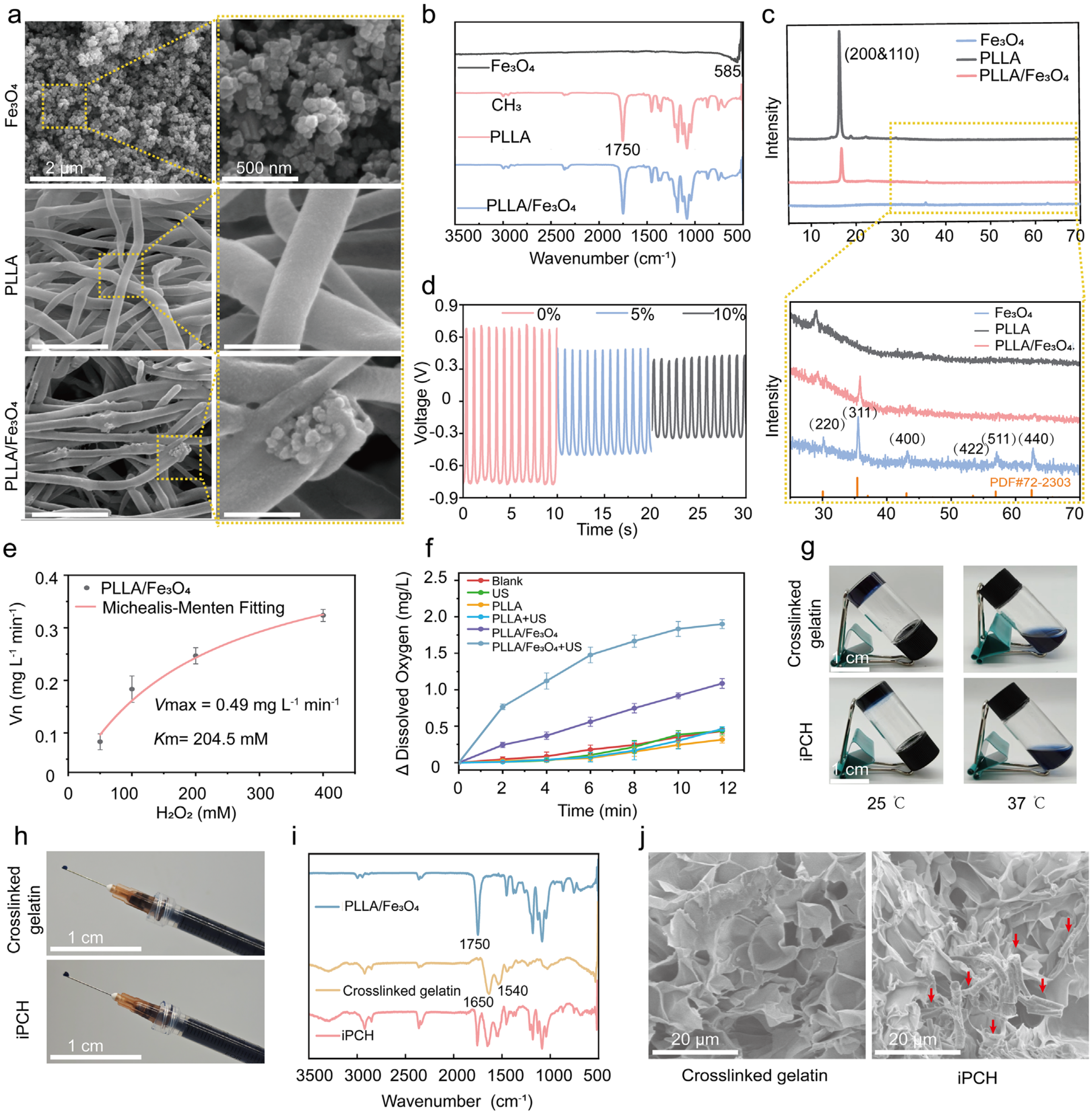

FIGURE 2 | Preparation and characterization of the US-excited iPCH. (a) SEM images of the Fe_3O_4, the annealed PLLA, the annealed PLLA/Fe_3O_4, scale bars: 2 μm in low-magnification and 500 nm in high-magnification. (b) FT-IR patterns and (c) XRD patterns of the Fe_3O_4, the annealed PLLA, and the annealed PLLA/Fe_3O_4. (d) Output voltage waveform of annealed PLLA/Fe_3O_4 with different Fe_3O_4 ratios. (e) Michaelis–Menten kinetics of PLLA/Fe_3O_4. (f) Time course of O_2 generation. (g) The crosslinked gelatin hydrogel and the US-excited iPCH at different temperatures, scale bars: 1 cm. (h) The injectability of the crosslinked gelatin hydrogel and the US-excited iPCH, scale bars: 1 cm. (i) FT-IR patterns and j) SEM images of the crosslinked gelatin hydrogel and the US-excited iPCH, scale bars: 20 μm, red arrow: PLLA/Fe_3O_4 short fibers. e, f: $n = 3$ independent samples. All statistical analyses were performed by one-way ANOVA. Data are presented as mean ± SD.

stimulation of PLLA excited by US [39, 40], which generated charge carriers that can accelerate the catalytic reaction process by enhancing the electron transfer efficiency between Fe_3O_4 nanozymes and H_2O_2 substrate, thereby enhancing its catalase-like activity [41].

To achieve in situ injection of PLLA/Fe_3O_4 short fibers in the flap repair area, these fibers were incorporated into an injectable crosslinked gelatin-based hydrogel, constructing the US-excited iPCH (Figures S5 and S6). Crosslinked gelatin was prepared based on the principle of nucleophilic addition between the C═C of Genipin and the -NH_2 of gelatin to form C─N bonds. FT-IR spectra showed that, compared with gelatin, the N─H band in the crosslinked gelatin shifted from 1245 to 1240 cm^{-1}, a result of successful crosslinking of gelatin with Genipin (Figure S6) [42]. Furthermore, gelatin significantly reduces the surface energy of PLLA, thereby improving the hydrophobicity of PLLA/Fe_3O_4 and ensuring its uniform dispersion [35]. The US-excited iPCH possessed both biocompatibility and temperature-responsive features, and exhibited typical temperature-sensitive behavior: at room temperature (25°C), the hydrogel stayed in a stable gel state, facilitating storage and transportation; when the temperature increased to physiological body temperature (37°C), it rapidly transformed into a fluid sol state, enabling wrapping of the wound bed (Figure 2g). As the shear rate increases (25°C), the viscosity of iPCH is decreased, this shear-thinning behavior enables in situ injection of the US-excited iPCH at the impaired area of the flaps (Figure S5; Figure 2h). FT-IR spectra showed that cross-linked gelatin exhibited characteristic absorption peaks at ~1650 cm^{-1} (amide I band, C═O stretching vibration) and ~1540 cm^{-1} (amide II band, N─H bending vibration and C─N stretching vibration), and the characteristic peaks PLLA/Fe_3O_4 were located at ~1750 cm^{-1} (C═O stretching vibration) and ~1500–1000 cm^{-1} (C─O─C stretching vibration). In the iPCH spectrum, the characteristic peaks of both components were clearly preserved (Figure 2i). Scanning electron microscopy (SEM) observations showed that the PLLA/Fe_3O_4 short fibers were uniformly dispersed in the hydrogel, with no obvious agglomeration (Figure 2j). These chemical compositions and microscopic morphological evidences together confirmed that PLLA/Fe_3O_4 could achieve a stable and uniform composite with crosslinked gelatin. Cell Counting Kit-8 (CCK-8) viability assays using human umbilical vein endothelial cells (HUVECs) demonstrated that the iPCH had no effect on cell survival, indicating its good biocompatibility (Figure S7).

2.2 | Piezoelectric Stimulation Generated by US-Excited iPCH Promoted Vascularization In Vitro

Flap survival is highly correlated with the reconstruction of blood vessels in the recipient area. Impaired angiogenesis leads to ischemia and hypoxia, ultimately resulting in flap necrosis [43]. ES has been proven to promote angiogenesis by promoting cell proliferation and migration of vascular endothelial cells [44–47]. To verify whether piezoelectric stimulation generated by the US-excited iPCH could promote angiogenesis, HUVECs were divided into the Blank group, the US group, the iPCH group, and the iPCH + US group (piezoelectric stimulation). Calcein acetoxymethyl ester (Calcein-AM) / propidium iodide (PI) staining and CCK-8 assay were used to evaluate the proliferation of HUVECs. On the third day, the cell viability exhibited no statistically significant difference among the US group, the iPCH group, and the Blank group (p >0.05). In contrast, the cell viability in the iPCH + US group was significantly higher than that in all other groups, reaching ~1.5 times of that in the iPCH and US groups (Figure 3a,b). This confirmed the piezoelectric stimulation generated by the US-excited iPCH could effectively promote the proliferation of HUVECs, which is key to building a functional vascular network.

A key event in angiogenesis is the migration of endothelial cells into the perivascular extracellular matrix [48, 49]. The results of scratch assays showed that the wound healing rate of the iPCH + US group at 12 h was ~51.2%, significantly higher than that of the Blank group (~29.4%), the US group (~33.2%), and the iPCH group (~29.3%). After 24 h of intervention, there was no statistically significant difference (p >0.05) in wound healing rates between the iPCH group (~71.4%), the US group (~73.9%), and the Blank group (~70.7%), while the wound healing rate of the iPCH + US group further increased to ~91.9% (Figure 3c,d). These results confirmed that the US-excited iPCH could effectively enhance the migration of HUVECs due to the piezoelectric stimulation, independent of US or PLLA regulation.

The ultimate goal of endothelial cell proliferation and migration is to drive the vascularization process. Vascular endothelial growth factor-A (VEGF-A) is a key cytokine regulating angiogenesis [50], and its expression directly reflects the ability of endothelial cells to form new vascular networks [51]. The expression level of VEGF-A was detected by immunofluorescence staining to verify the regulatory effect of piezoelectric stimulation generated by the US-excited iPCH on angiogenesis (Figure 3e,f). The mean fluorescence intensity of VEGF-A in the US group was slightly higher than that in the Blank group and the iPCH group, but there was no statistical difference (p >0.05); while the mean fluorescence intensity of the iPCH + US group was ~1.5 times that of the iPCH group. These results confirmed the positive role of piezoelectric stimulation generated by US-excited iPCH in the regulation of angiogenesis. It not only directly drove the proliferation and migration of HUVECs, but also activated the angiogenesis cascade of HUVECs at the molecular level by specifically upregulating the expression of the pro-angiogenic factor, demonstrating potential to accelerate the construction of functional neovascular networks.

2.3 | Reversal of H_2O_2-Induced Oxidative Stress by the US-Excited iPCH In Vitro

ROS scavenging can alleviate oxidative stress and inflammatory response, and is crucial for improving flap survival [11, 12, 52, 53]. To simulate the impact of the oxidative stress microenvironment on angiogenesis in diabetic flaps in vitro, we exposed the HUVECs to different H_2O_2 concentrations (0, 50, 100, 200 μM), and then assessed cell viability with CCK-8 assay. As the H_2O_2 concentration increased, the viability of HUVECs decreased. When the H_2O_2 concentration reached 200 μM, the viability of endothelial cells was significantly inhibited (reduced to ~53.8% of the normal group) (Figure S8), and this concentration was selected as the oxidative stress model. To ensure the ability of the US-excited iPCH to scavenge H_2O_2 and maintain endothelial cell viability in an oxidative stress microenvironment, we set up the Blank group without H_2O_2 exposure, and the H_2O_2 group, the US group, the iPCH group, and the iPCH + US group all of which were exposed to 200 μM H_2O_2, then we used Calcein-AM/PI staining and the CCK-8 for assessments (Figure 4a). The Calcein-AM/PI staining images showed that endothelial cells simply exposed to H_2O_2 or treated with US exhibited more red fluorescence (dead cells) and less green fluorescence (live cells), indicating that US could not scavenge H_2O_2 in the microenvironment. In contrast, after introducing iPCH, the proportion of live cells increased significantly. The results of CCK-8 assay further confirmed the protective effect of iPCH. The relative cell viability of the iPCH group and the iPCH + US group were ~79.4% and ~90.7% of the Blank group, respectively, both significantly higher than that of the H_2O_2 group (~51.1%) (Figure 4b). Furthermore, the cell viability of the iPCH + US group was slightly higher than that

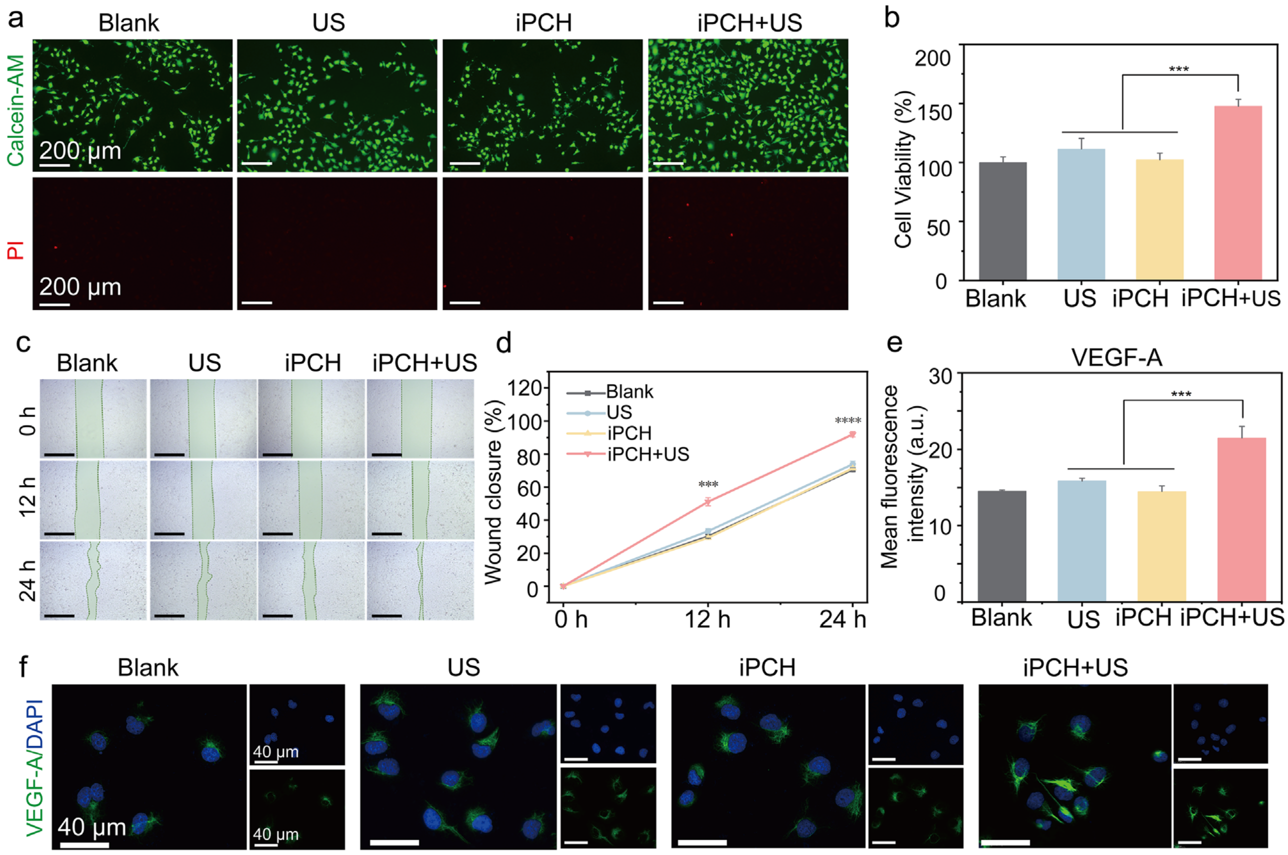

FIGURE 3 | Effect of the US-excited iPCH on vascularization. (a) Live/dead staining of HUVECs under normal microenvironment, scale bars: 200 μm. (b) Cell viability of HUVECs. (c) Images of the scratch test at 0, 12, and 24 h. (d) Wound healing rate in scratch assay, scale bars: 500 μm. (e) Quantitative analysis of VEGF-A mean fluorescence intensity. (f) VEGF-A immunofluorescence staining, scale bars: 40 μm. b, d, e: $n = 3$ independent samples. ***$p < 0.001$ and ****$p < 0.0001$. All statistical analyses were performed by one-way ANOVA. Data are presented as mean ± SD.

of the iPCH group ($p > 0.05$), which might be the piezoelectricity generated by the US-excited iPCH that enhanced the catalytic activity of Fe_3O_4 nanozymes, thereby further improving the scavenging efficiency of H_2O_2.

Subsequently, we used Calcein-AM/PI staining and the CCK-8 assay to evaluate the continued survival and proliferation recovery capacity of surviving HUVECs after reversing the oxidative stress microenvironment (Figure 4c,d). The results showed that cell survival in the H_2O_2 group was significantly limited (only ~63.6%), while both the iPCH and iPCH+US groups exhibited significant anti-damage protective effects, with survival rates recovering to ~84.8% and ~90.0%, respectively. These results confirmed that the antioxidant properties of iPCH could effectively improve the local oxidative stress microenvironment, resisting oxidative damage to endothelial cells by reducing ROS levels, thereby maintaining the viability and proliferation capacity of the vascular endothelial cells.

In addition, immunofluorescence staining of Ki-67 confirmed that its expression trend was consistent with the results of the CCK-8 assay: the mean fluorescence intensity of Ki-67 in the H_2O_2 group (~27.9 a.u.) was only ~64.7% of that in the Blank group (~43.1 a.u.); the mean fluorescence intensity of Ki-67 in the iPCH + US group (~39.2 a.u.) and the iPCH group (~37.8 a.u.) were ~91% and ~88% of that in the Blank group (Figure 4e,f) [54]. These results indicated that the oxidative stress microenvironment significantly downregulated the expression of the cell proliferation marker Ki-67; while iPCH, through the free radical scavenging properties of Fe_3O_4 nanozymes, effectively resisted the arrest of the cell proliferation cycle by oxidative damage [54].

In summary, iPCH could not only scavenge H_2O_2 in the microenvironment to maintain the survival rate and continued proliferation of vascular endothelial cells, but also generate piezoelectric stimulation under US excitation to promote the proliferation, migration, and vascularization of vascular endothelial cells, showing potential to improve the survival of diabetic flaps (Figure 4g).

2.4 | The US-Excited iPCH Improves Flap Survival in Diabetic Rats via ROS Scavenging and Angiogenesis Promotion

A skin flap transplantation model was established in diabetic rats to further evaluate the ability of the US-excited iPCH to promote angiogenesis and flap survival (Figure 5a). The US-excited iPCH not only provided piezoelectric stimulation but also generated oxygen in situ after H_2O_2 scavenging. To compare its therapeutic effect with that of single electrical stimulation, we prepared an

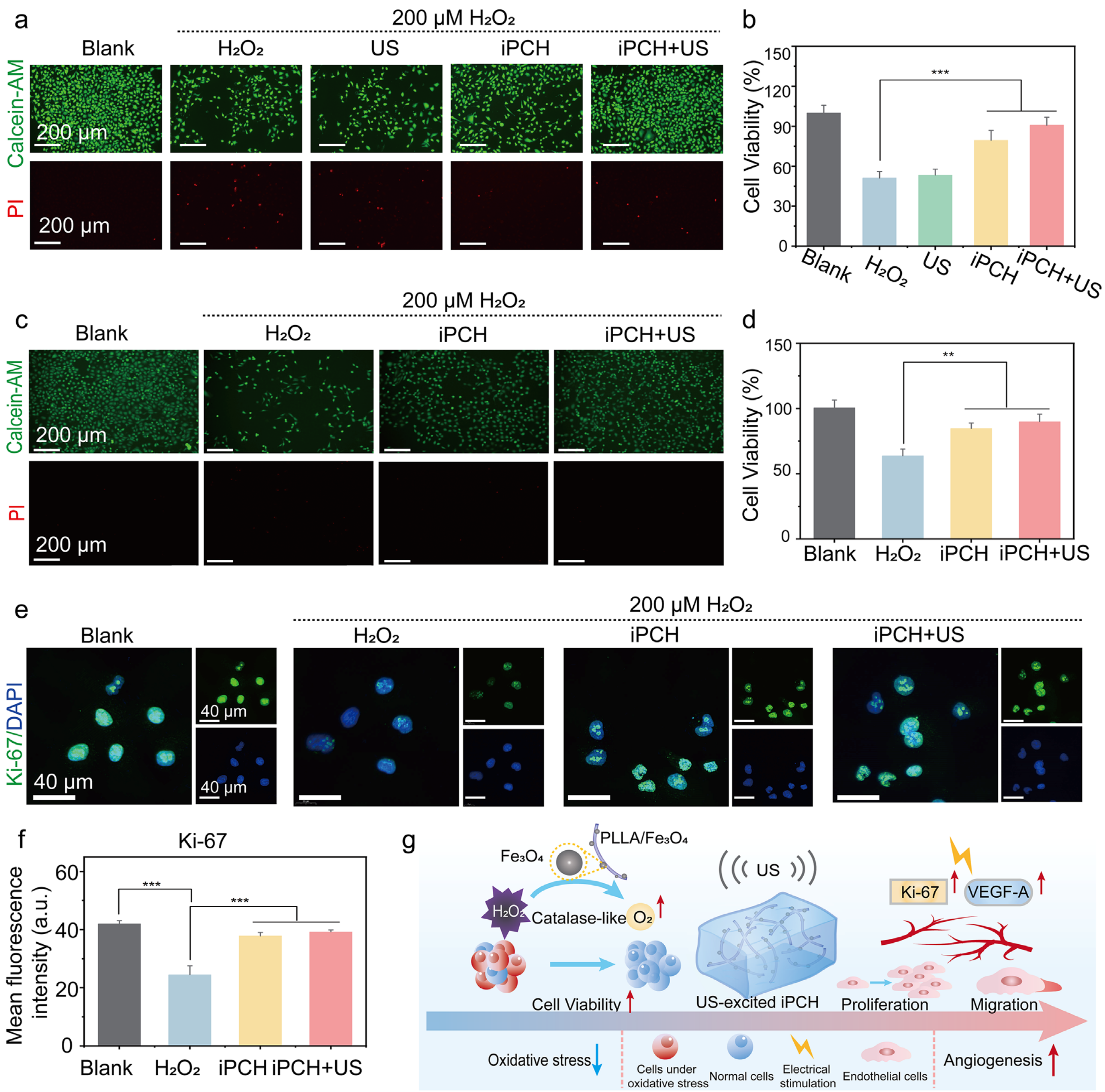

FIGURE 4 | Effect of the US-excited iPCH on oxidative stress microenvironment in vitro. (a) Live/dead staining of HUVECs under oxidative stress microenvironment, scale bars: 200 μm. (b) Cell viability of HUVECs under an oxidative stress microenvironment. (c) Live/dead staining of HUVECs after oxidative stress pretreatment, scale bars: 200 μm. (d) Cell viability of HUVECs after oxidative stress pretreatment. (e) Ki-67 immunofluorescence staining, scale bars: 40 μm. (f) Quantitative analysis of Ki-67 mean fluorescence intensity. (g) Schematic diagram of the in vitro experiments of the US-excited iPCH. b, d, f: $n = 3$ independent samples. $^{**}p < 0.01$ and $^{***}p < 0.001$. All statistical analyses were performed by one-way ANOVA. Data are presented as mean ± SD.

injectable piezoelectric crosslinked gelatin-based hydrogel (iPG) by adding PLLA instead of PLLA/Fe_3O_4 to the crosslinked gelatin-based hydrogel; the iPG can generate ES excited by the US but lacks H_2O_2 scavenging capacity. Diabetic model rats were divided into four groups: the Control group, the iPG + US group, the iPCH group, and the iPCH + US group. From the macroscopic morphological characteristics, the surviving and necrotic skin flaps have significant distinguishability: necrotic skin flaps gradually form scabs, become harder in texture, and darken in color, eventually falling off; while the surviving skin flaps maintain a soft texture and normal tissue color, with no obvious signs of necrosis [8]. The skin flaps in the Control group showed an obvious necrosis (~54.4%) on the third day after the operation, and the necrotic area of the skin flap exceeded ~85.5% on the seventh day after the operation; while the necrosis rate of the iPCH + US group was 16.0% on the third day, and only increased to ~39.2% on the seventh day, significantly lower than those of the iPG + US group (~62.3%) and the iPCH group (~59.3%) (Figure 5b,c). These results confirmed that the synergistic effect of piezoelectric stimulation and H_2O_2-scavenging capacity of the US-excited iPCH could effectively improve the survival prognosis of diabetic skin flaps.

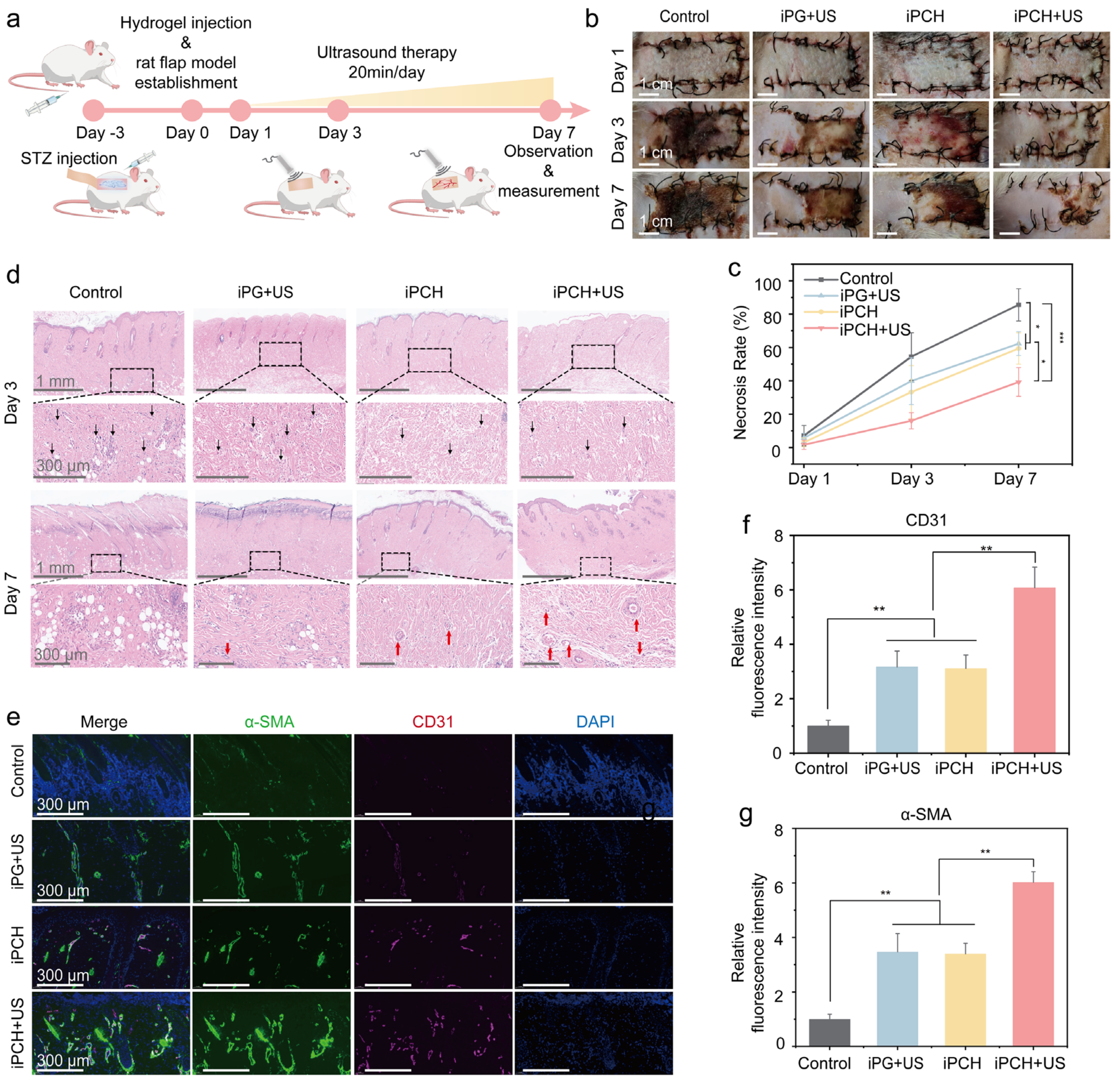

FIGURE 5 | Therapeutic efficacies of the US-excited iPCH on diabetic flaps. (a) Schematic diagram of animal experimental procedure. (b) Images of diabetic flaps in rats, scale bars: 1 cm. (c) Necrosis rate statistics. (d) H&E staining of diabetic flaps, scale bars: 1 mm in low-magnification and 300 μm in high-magnification, black arrow: inflammatory cells, red arrow: new vessels. (e) Immunofluorescence staining of diabetic flaps, scale bars: 300 μm. (f) Quantitative analysis of CD31 relative fluorescence intensity. (g) Quantitative analysis of α-SMA relative fluorescence intensity. c, f, g: $n = 3$ independent samples. *$p < 0.05$, **$p < 0.01$ and ***$p < 0.001$. All statistical analyses were performed by one-way ANOVA. Data are presented as mean ± SD.

The histopathological staining further revealed the microscopic structure of the skin flaps (Figure 5d). In the Control group on the third day after the operation, the collagen fibers of the skin flap tissue were disordered, exhibiting numerous foamy tissue cells (containing inflammatory cells and necrotic cells). This suggested a severe local inflammatory response and tissue necrosis, consistent with the ROS accumulation and persistent inflammation caused by the high glucose microenvironment of diabetes. The densities of inflammatory cells in the iPCH group and the iPCH + US group were ~26 pieces/0.1 mm^2 and ~21 pieces/0.1 mm^2, respectively. It indicated that iPCH, through the Fe_3O_4 nanozymes loading, scavenged the large amount of ROS accumulated in the early stages of injury, reducing the inflammatory response at the injury site, and could generate trace amounts of oxygen in situ, creating a favorable microenvironment for flap survival. Although the necrosis rate of the flap in the iPG + US group was low, the number of inflammatory cells infiltrating the flap was high (~53 pieces/0.1 mm^2) due to its poor ability to scavenge ROS, which was close to that in the Control group (~59 pieces/0.1 mm^2). The survival rate of flaps is positively correlated with the formation of new vascular networks [55]. We speculated that the smaller necrotic area of flaps in the iPG + US group might be related to the promotion of local vascular network formation by piezoelectric stimulation under US excitation. Therefore, we stained the flap tissue with H&E staining on the seventh day after the operation. In the flap tissue of the iPG + US group, intact epithelial structures, abundant neovascularization, and well-arranged collagen fibers could be observed. The density of new vessels in the iPG + US group was ~3.1 times that of the Control group, while that in the iPCH + US group was even higher, which was ~1.8 times that of the iPG + US group, and ~2.0 times that of the iPCH group. Compared to piezoelectric stimulation or ROS scavenging, the US-excited iPCH could simultaneously reduce inflammatory cell infiltration and promote angiogenesis in diabetic flaps, thus providing more favorable conditions for skin flap survival (Figures S9 and S10). Furthermore, we confirmed that iPCH had good biodegradability in vivo. Pathological section images showed that there was a small area of iPCH residue on the 14th day, while the crosslinked gelatin matrix of iPCH was almost completely degraded on the 28th day (Figure S11).

Immunofluorescence staining of alpha-smooth muscle actin (α-SMA) and platelet endothelial cell adhesion molecule-1 (CD31) further validated the ability of iPCH to promote angiogenesis (Figure 5e). CD31 is a core indicator for characterizing vascular density; α-SMA serves as a specific marker for pericytes/vascular smooth muscle cells, whose expression level directly reflects the structural maturity of new blood vessels [56, 57]. The results showed that the fluorescence intensity of CD31 in the iPCH and the iPG + US groups was ~3.1 times and ~3.2 times that of the Control group, while the fluorescence intensity of CD31 in the iPCH + US group was significantly enhanced, ~1.9 times that of the iPG + US groups. The results were similar to those obtained from HE staining. Consistently, the immunofluorescence staining of α-SMA showed that the iPG + US group was ~3.5 times that of the Control group, the iPCH group was ~3.4 times that of the Control group, and the iPCH + US group exhibited the highest fluorescence expression, was ~1.7 times that of the iPG + US groups (Figure 5f,g). These results suggested that US-excited iPCH could not only promote angiogenesis in diabetic flaps but also accelerate vascular maturation, which might be one of the reasons why iPCH significantly improves the survival rate of diabetic flaps.

2.5 | Molecular Biological Mechanism Study of US-Excited iPCH Promoting the Survival of Diabetic Flaps

To further elucidate the molecular mechanism, we conducted transcriptome sequencing analysis on the flap tissues of the Control group and the iPCH + US group. The results of the volcano map and heat map showed that a total of 210 differentially expressed genes were identified between the two groups, including 24 upregulated genes and 186 downregulated genes (Figure 6a,b). Gene Ontology (GO) enrichment analysis demonstrated that genes closely related to angiogenesis and tissue repair, such as *Flrt2* and *Pgf*, were upregulated, indicating the potential of the US-excited iPCH in angiogenesis (Figure 6c).

In addition, the GO enrichment analysis demonstrated that key genes in inflammatory response were downregulated (*Cxcl2, Il23a)* (Figure 6d). Previous studies have confirmed that ROS upregulate the expression of *Cxcl2* and *Il23a* [58, 59]; and promote the secretion of IL-1β and TNF-α [60, 61], thereby activating the inflammatory cascade. They reflect the intensity and duration of local inflammatory cell infiltration. To verify that iPCH has the ability to inhibit this cascade, we performed immunofluorescence staining for IL-1β and TNF-α was performed on the flap tissues to clarify the differences in the inflammatory microenvironment of each group of flaps (Figure 6e–i). The results showed that the IL-1β expression level in the iPG + US group, which only received piezoelectric stimulation, was ~7.5 times that of the iPCH + US group, and the TNF-α expression level was ~15.1 times that of the iPCH + US group, confirming that piezoelectric stimulation cannot effectively inhibit the inflammatory cascade under the adverse conditions of ROS accumulation. In contrast, the iPCH group and the iPCH + US group, which possess ROS clearance capabilities, exhibited better anti-inflammatory effects. This significant improvement in the inflammatory phenotype was attributed to the efficient removal of local ROS by iPCH. In summary, US-excited iPCH could break the vicious cycle of “ROS accumulation-inflammatory amplification”, and effectively reduce the early inflammatory response induced by oxidative stress. The successful reversal of this inflammatory microenvironment is one of the key mechanisms by which the synergistic strategy based on iPCH ultimately improved the survival prognosis of diabetic flaps.

3 | Conclusion

We developed the US-excited iPCH in this study, which ameliorated the long-standing inflammation microenvironment induced by the persistent hyperglycemic state, promoted angiogenesis of diabetic wounds, and effectively improved the survival rate of diabetic flaps. During treatment, the US-excited iPCH exhibited a clear temporal regulatory effect: First, the generated piezoelectric charges accelerated electron transfer on the surface of Fe_3O_4 nanozymes through the piezoelectric effect, significantly improving their efficiency in scavenging H_2O_2. This improved the long-standing oxidative stress microenvironment in diabetic flaps, reduced the expression of inflammatory factors such as IL-1β and TNF-α, and increased the survival of endothelial cells. Subsequently, in the improved microenvironment, vascular endothelial cells rapidly proliferated and migrated under the piezoelectric stimulation generated by the US-excited iPCH, which ultimately promoted vascular reperfusion of the transplanted flaps and improved flap survival. This strategy provides a safer, more cost-effective, and more efficient novel therapeutic approach for clinically improving the survival of diabetic flaps, which is expected to enhance the rehabilitation efficacy and quality of life of patients.

4 | Experimental Section

4.1 | Preparation of Fe_3O_4

The entire process was carried out under a nitrogen-protected atmosphere, and the distilled water used was pre-boiled for 30 min to remove dissolved oxygen. 560 mL of 0.3 mol/L iron(II) sulfate solution (F116341, Aladdin) was preheated to 90°C, followed by the dropwise addition of 240 mL of a mixed solution containing 3.33 mol/L potassium hydroxide (T197216, Aladdin) and 0.27 mol/L potassium nitrate (P117721, Aladdin) within several min. The resulting suspension was continuously heated and stirred at 90°C for 60 min. Then cooled, the precipitate was collected by centrifugation, and washed with distilled water

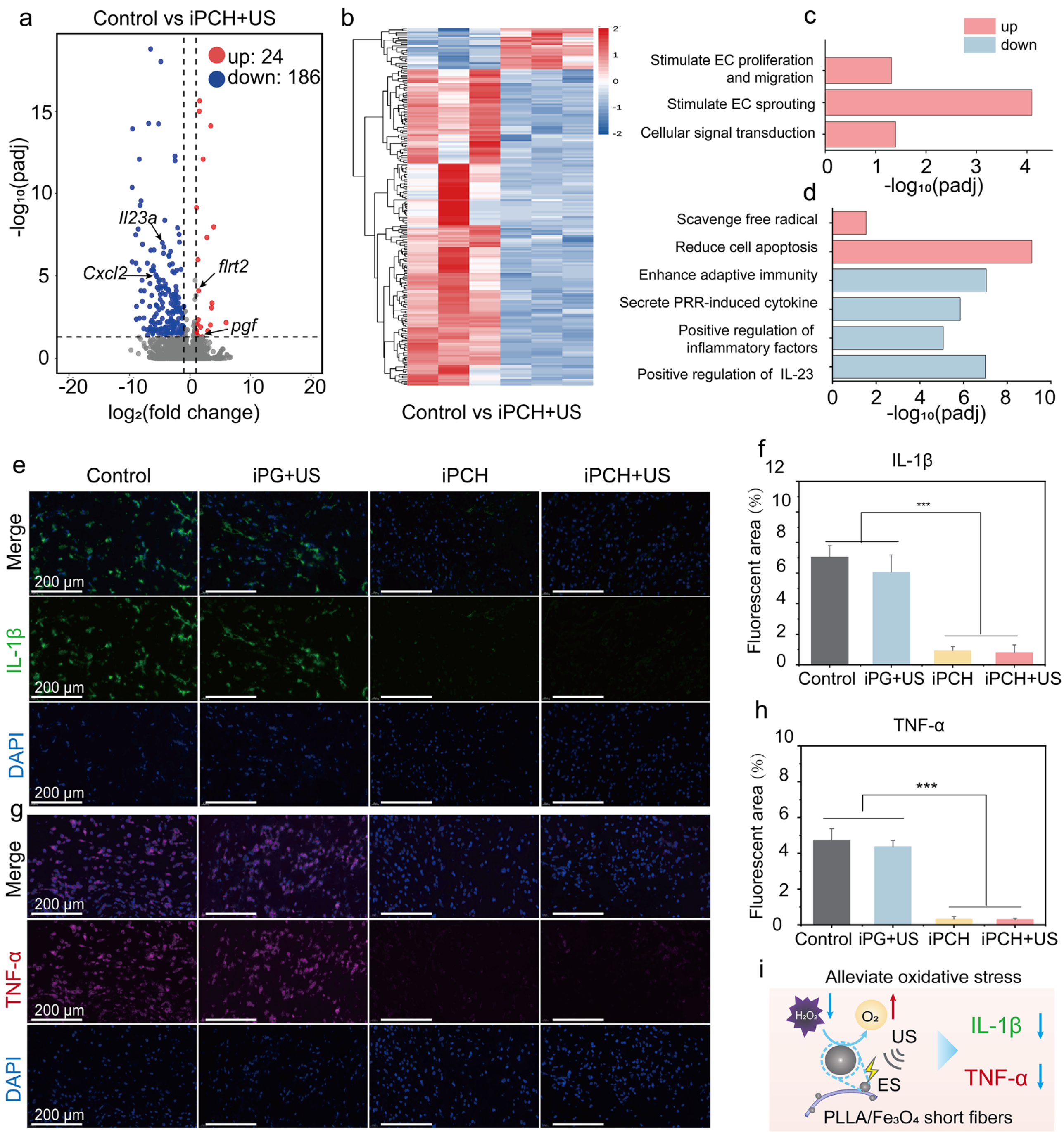

FIGURE 6 | Transcriptome analysis and effect of the US-excited iPCH on inflammation. (a) Volcano plot of differential expression genes. (b) Heatmap of differential expression genes. (c,d) GO enrichment analysis of angiogenesis and inflammation. (e,f) Immunofluorescence staining and fluorescence area analysis of IL-1β. (g,h) Immunofluorescence staining and fluorescence area analysis of TNF-α. e, g: scale bars: 200 μm. (i) Schematic diagram of US-excited iPCH in alleviating oxidative stress. f, h: $n = 3$ independent samples. $^{***}p < 0.001$. All statistical analyses were performed by one-way ANOVA. Data are presented as mean ± SD.

four times. The sample was freeze-dried and stored as a solid for future use.

4.2 | Preparation of Piezoelectric PLLA Nanofiber Membranes via Electrospinning

1 g of PLLA (PLLA-15, 1.00-1.50 dL/g, Boli Biomaterials) was weighed and dissolved in 5 mL of hexafluoroisopropanol (H107503, Aladdin), stirring at room temperature for 4 h to prepare the spinning solution. Transfer the solution to an injection syringe. The spinning solution delivery rate was set to 1 mL per hour, and the spin for 40 min. The solution was extruded through a G22 needle with a positive voltage of 13 kV applied, collected on an aluminum foil-coated receiving roller rotating at 2000 revolutions per min to obtain an aligned nanofiber membrane. A negative voltage of −2 kV was applied to the receiving roller, and the ambient relative humidity was controlled within the range of

30 ± 10%. The PLLA nanofiber membrane was annealed at 120°C for 6 h and slowly cooled to room temperature.

4.3 | Preparation of Piezoelectric PLLA/Fe_3O_4 Nanofiber Membranes via Electrospinning

1 g of PLLA was weighed and dissolved in 5 mL of hexafluoroisopropanol together with 50, 100 mg of Fe_3O_4 (corresponding to 5 and 10 wt.%), stirring at room temperature for 4 h. All other electrospinning parameters were consistent with those used for the preparation of PLLA nanofiber membranes.

4.4 | Characterization of Nanofiber Membranes

The crystallinity was analyzed using the X-ray Powder Diffractometer (XRD, Xpert3 Powder), and the chemical composition of the nanofiber membranes was characterized by Fourier Transform Infrared Spectrometer (FT-IR, VERTEX80v, Bruker). The piezoelectric response was detected using an oscilloscope (Teledyne LeCroy HD 4096). Both sides of the nanofiber membrane were coated with conductive paint as electrodes. They were cut into 2.0 cm × 1.0 cm rectangles. Copper wires were soldered to the electrode ends, and the entire device was sealed with polytetrafluoroethylene (PTFE) tape to fabricate the Piezoelectric nanogenerator.

4.5 | Preparation and Characterization of PLLA and PLLA/Fe_3O_4 Piezoelectric Short Fibers

After annealing, the PLLA or PLLA/Fe_3O_4 nanofiber membrane was immersed in a cryoembedding agent (4583, SAKURA), and cut into short fibers with a length of 10 µm using a freezing microtome (CM3050S, Leica). They were washed with deionized water, and freeze-dried for 24 h. The Scanning Electron Microscopy (SEM) was used to observe their morphological and dimensional characteristics.

4.6 | Preparation of Crosslinked Gelatin Hydrogel

4 g of gelatin (G108395,250 g bloom, Aladdin) was weighed, and dissolved in 16 mL of deionized water, stirring at 65°C and 600 r/min for 24 h. 1.2 mL of Genipin (S110910, Aladdin) was added followed by stirring at 65°C for another 24 h at 500 r/min. The crosslinked gelatin hydrogel was prepared.

4.7 | Preparation of the iPG

4 g of gelatin was weighed, and dissolved in 16 mL of deionized water, stirring at 65°C and 600 r/min for 24 h. Added 1.2 mL of Genipin and 4 mg of PLLA Short Fibers, and stirred at 65°C for another 24 h at 500 r/min. The *iPG* was then prepared.

4.8 | Preparation of the US-Excited iPCH

4 g of gelatin was weighed, and dissolved in 16 mL of deionized water, followed by stirring at 65°C and 600 r/min for 24 h. Added 1.2 mL of Genipin and 4 mg of PLLA/ Fe_3O_4 Short Fibers, and stirred at 65°C for another 24 h at 500 r/min. The US-excited iPCH was then prepared.

4.9 | Characterization of Hydrogels

The injectability was evaluated using a 1 mL syringe (needle inner diameter: 0.33 mm). FT-IR (VERTEX80v, Bruker) was employed to verify the chemical composition of the hydrogel, and Scanning Electron Microscopy (SEM, SU8020) was used to observe the surface morphology of the hydrogel.

4.10 | Catalase-Like Activity

Oxygen generation in different groups was measured using a dissolved oxygen analyzer (ST300D, OHAUS) for 12 min in weakly alkaline phosphate buffered saline (PBS) buffer (pH 7.4). These groups included the Blank group, the Blank + US group, the PLLA group, the PLLA + US group, the PLLA/Fe_3O_4 group, and the PLLA/Fe_3O_4 + US group. The US parameters were set to 1 MHz and 0.5 W/cm^2, and the PLLA and PLLA/Fe_3O_4 concentration was both 50 µg/mL.

4.11 | Michaelis-Menten Kinetics

O_2 generation for 10 min in weakly alkaline PBS buffer (pH 7.4) containing PLLA/Fe_3O_4 (50 µg/mL) and different concentrations of H_2O_2 (50, 100, 200, 400 mM) was quantitatively determined using a dissolved oxygen analyzer (ST300D, OHAUS) to evaluate the Michaelis-Menten kinetics of PLLA/Fe_3O_4.

4.12 | Cell Culture

Human Umbilical Vein Endothelial Cells (HUVECs) were purchased from the Cell Bank of the Chinese Academy of Sciences (Beijing). The cells were cultured in high-glucose DMEM medium (11995, Solarbio) and supplemented with 10% fetal bovine serum (FBS, Gibco) with 1% penicillin-streptomycin double antibody (P1400, Solarbio). The cells were cultured in an incubator (CCL-170B-8, ESCO) at 37°C with 5% CO_2.

4.13 | In Vitro Biocompatibility Experiment

After being double-sterilized by soaking in ethanol and ultraviolet (UV) irradiation, Samples were immersed in high-glucose DMEM medium for 24 h. The HUVECs were co-cultured with iPCH hydrogel leachates of different concentrations (0, 25, 50, 75, 100%) in 96-well plates for 24 h, and Cell Counting Kit-8 (CCK-8, CA1210, Solarbio) was used to detect cell viability. Absorbance of the supernatant after the reaction between CCK-8 was measured using a microplate reader (BioRad iMark) at a wavelength of 450 nm.

4.14 | In Vitro HUVECs Viability Assay

HUVECs were seeded in 24-well plates. After 12 h of culture, the iPCH, sterilizing with ethanol and UV light, was added, followed by US treatment (1 MHz, 0.5 W/cm^2, 2 min/6 h, ultrasonic gel). Cells were harvested at 72 h, and cell proliferation was assessed using CCK-8 assay (CA1210, Solarbio) to measure absorbance and Calcein-AM/PI (CA1630, Solarbio) to measure fluorescence intensity.

4.15 | HUVECs Cell Viability Assay Under In Vitro Oxidative Stress Microenvironment

HUVECs were seeded in 24-well plates. After 12 h of culture, the US-excited iPCH sterilized with ethanol and UV light was added, followed by the addition of 200 μM H_2O_2 and US treatment (1 MHz, 0.5 W/cm^2, 2 min/6 h, ultrasonic gel). Cells were harvested after 24 h, and absorbance was measured using the CCK-8 assay (CA1210, Solarbio), while fluorescence intensity was measured using the Calcein-AM/PI assay (CA1630, Solarbio) to assess cell proliferation.

4.16 | HUVECs Cell Viability Assay After In Vitro Oxidative Stress Pretreatment

HUVECs were seeded in 24-well plates. After 12 h of culture, the iPCH, sterilizing with ethanol and UV light, was added, followed by 200 μM H_2O_2 and US treatment (1 MHz, 0.5 W/cm^2, 2 min/6 h, ultrasonic gel). After 24 h, the medium was replaced with fresh medium and cultured for another 24 h. The absorbance was measured using the CCK-8 assay (CA1210, Solarbio), and the fluorescence intensity was measured using the Calcein-AM/PI assay (CA1630, Solarbio) to assess cell proliferation.

4.17 | Scratch Assay

Cells were cultured in 24-well plates and scratched using a 1.5 mL pipette tip. Subsequently, iPCH was added and co-cultured with the cells, followed by sonication (1 MHz, 0.5 W/cm^2, 2 min/6 h, ultrasonic gel). Time-lapse images of the cells were captured at 0, 12, and 24 h. Image J software was used to quantitatively analyze the images and assess cell migration.

4.18 | Cell Immunofluorescence Staining

Fixed cells with 4% paraformaldehyde (P1110, Solarbio) for 15 min and then washed three times with 1×PBS buffer. The cells were blocked with a blocking solution at room temperature for 2 h. The blocking solution contained 3% bovine serum albumin (BSA, SW3015, Solarbio), 10% FBS (10099-141, Gibco), and 0.5% Triton X-100 (T8200, Solarbio). Primary antibodies Ki-67 antibody (9129, BASMEDTSCI, 1:100) and VEGF-A antibody (15165-100, CST, 1:100) were added and incubated at 4°C overnight. Fluorescent secondary antibodies were then added and incubated for 1 h at room temperature. The cell nuclei were stained with 4',6-diamidino-2-phenylindole (DAPI, 1:200, c0060, Solarbio) for 10 min. Capture fluorescent images of cells using a confocal laser scanning microscope (Leica, SP8), and the fluorescence intensity or positive expression rate was analyzed using Image J software.

4.19 | Animal Culture

40 male SD rats with no health disorders and a body weight of approximately 250 g (8-week-old) were selected as experimental animals. The rats were raised in the Animal Center of Beijing Institute of Nanoenergy and Nanosystems under a Specific Pathogen-Free (SPF) environment with the temperature controlled at 25°C. General anesthesia and analgesia were performed on the rats in accordance with the "Experimental Animal Operation Guidelines" formulated by the Animal Resources Committee. All animal procedures were approved by the Committee on Ethics of Small Animal Experimental Platform of National Key Laboratory (Approval No.: 2025004LZ) and strictly followed the ARRIVE guidelines for in vivo animal research reports.

4.20 | In Vivo Animal Experiment

3 days before the operation, a diabetic rat model was established by intraperitoneal injection of streptozotocin (STZ) at 50 mg/kg after fasting for 12 h, with daily blood glucose monitoring; a blood glucose level ≥16.7 mmol/L was regarded as the criterion for successful modeling. Diabetic model rats were divided into four groups: the Control group (Sham, diabetic model rats receiving only sham operation), the iPG + US group (ES), the iPCH group (H_2O_2 scavenging), and the iPCH + US group (ES and H_2O_2 scavenging). On the day of the operation, the rats were anesthetized with 2% isoflurane gas, and the hair on the back of the rats was removed with electric clippers and depilatory cream. An intermittent suture method was used to construct a rat dorsal skin flaps transplantation model (4.5 × 1.5 cm), and hydrogel injection and/or US intervention were performed in each corresponding experimental group. The iPG + US group and iPCH + US group received daily US stimulation (1 MHz, 0.5 W/cm^2, two 10 min US separated by a 10 min rest interval, ultrasonic gel), which was within the safe range of clinical US treatment and could effectively excite the piezoelectric effect. All materials were sterilized by pasteurization and injected using a 1 mL syringe (needle inner diameter: 0.33 mm). The US treatment cycle was 1 week, adopting an intervention mode of 1 day rest after the operation and 6 consecutive days of US treatment. On the first, third, and seventh days after the operation, the appearance photos of the rat skin flaps were observed and recorded with a digital camera for flaps morphology observation and survival rate calculation. On the third and seventh days after the operation, the rat skin flaps tissues were collected to prepare pathological sections.

4.21 | Histological Examination

The obtained skin flaps tissues were fixed with 4% paraformaldehyde, dehydrated with gradient ethanol, and embedded in paraffin to prepare continuous sections, which were then subjected to Hematoxylin-Eosin (H&E) staining and immunofluorescence staining in sequence. Antibodies used in the immunofluorescence staining: CD31 (ab182981, abcam, 1:2000), α-SMA (ab124964, abcam, 1: 5000), IL-1β (26048-1-AP, PTG, 1: 400), TNF-α (BA0131, boster, dilution ratio: 1:400). The staining results were quantitatively analyzed using Image J software after microscopic observation.

4.22 | Transcriptome Sequencing and Data Analysis

Skin flaps tissues were collected third after the operation. Total RNA was extracted from the wound tissues using an RNA extraction kit (TIANGEN, Cat. No. DP424), followed by RNA sequencing with Illumina Xplus(PE150, Yike Tianya Biotechnology (Chongqing, China) was responsible for quality control, comparison, and quantification of the raw RNA sequencing data. R (Version 3.0.3) was used for conducting RNA-seq expression data analysis. A minimum two- fold change and a Padj cutoff < 0.05 was applied as filtering criteria.

4.23 | Statistical Analysis

One-way analysis of variance (one-way ANOVA) was used to compare the statistically significant differences between groups. The cell experiments were independently repeated three times. And the results of H&E staining and immunofluorescence staining of skin flaps tissues were all derived from parallel experimental data of 3 animal models. Data were analyzed using GraphPad Prism 9.0, and the results were expressed as mean ± Standard deviation (Mean ± SD). Data visualization was performed using Image J (Media Cybernetics, USA) and Origin 2021 (OriginLab, USA). $^{*}p < 0.05$, $^{**}p < 0.01$, and $^{***}p < 0.001$ indicated statistically significant differences.

Author Contributions

Mingcheng Tang and Ruizeng Luo conceived the concept, processed the structure details carried out experiments, and wrote the manuscript. Jiaping Zhang and Zhou Li revised the manuscript and supervised the work. Yunfan Tang and Baokun Zhang assisted in the cell experiments. Puqing Yao and Qiao Yu assisted in the characterization and photography of sample images. Kun Fang and Yong Chen assisted in the animal experiments. All authors commented on the submitted version of the manuscript.

Acknowledgements

Mingcheng Tang and Ruizeng Luo contributed equally to this work. The authors thank the support received from the National Natural Science Foundation of China (T2125003, U25A20417, 82272285), Beijing Natural Science Foundation (L245015, Z240022, 25JL006), Chongqing Natural Science Foundation (2024NSCQ-KJFZZDX0015), Chongqing Leading Medical Talents Project (424Z28E2, YXLJ202414), Chongqing Key Clinical Specialties Construction Project (524Z2M71), and the Fundamental Research Funds for the Central Universities.

Funding

This research was supported by the National Natural Science Foundation of China (T2125003, U25A20417, 82272285), Beijing Natural Science Foundation (L245015, Z240022, 25JL006), Chongqing Natural Science Foundation (2024NSCQ-KJFZZDX0015), Chongqing Leading Medical Talents Project (424Z28E2, YXLJ202414), Chongqing Key Clinical Specialties Construction Project (524Z2M71), and the Fundamental Research Funds for the Central Universities.

Conflicts of Interest

The authors declare no conflicts of interest.

Data Availability Statement

The data that support the findings of this study are available from the corresponding author upon reasonable request.

References

1. A. J. M. Reed, N. T. Y. Lim, S. W. L. Yip, et al., "Outcomes of Flap Reconstruction for Diabetic Foot Ulcers: A Systematic Review and Meta-Analysis of Clinical Studies," *Plastic & Reconstructive Surgery* 154, no. 5 (2024): 1118–1130, https://doi.org/10.1097/prs.0000000000011231.

2. K. McDermott, M. Fang, A. J. M. Boulton, E. Selvin, and C. W. Hicks, "Etiology, Epidemiology, and Disparities in the Burden of Diabetic Foot Ulcers," *Diabetes Care* 46, no. 1 (2023): 209–221, https://doi.org/10.2337/dci22-0043.

3. B. Yang and J. Shi, "Ferrihydrite Nanoparticles Alleviate Rheumatoid Arthritis by Nanocatalytic Antioxidation and Oxygenation," *Nano Letters* 23, no. 17 (2023): 8355–8362, https://doi.org/10.1021/acs.nanolett.3c02743.

4. N. Yang, R. Hua, Y. Lai, et al., "Microenvironment-Adaptive Nanomedicine MXene Promotes Flap Survival by Inhibiting ROS Cascade and Endothelial Pyroptosis," *Journal of Nanobiotechnology* 23, no. 1 (2025): 282, https://doi.org/10.1186/s12951-025-03343-9.

5. D. B. Kitchen, H. Decornez, J. R. Furr, and J. Bajorath, "Docking and Scoring in Virtual Screening for Drug Discovery: Methods and Applications," *Nature Reviews Drug Discovery* 3, no. 11 (2004): 935–949, https://doi.org/10.1038/nrd1549.

6. A. M. Vincent, J. W. Russell, P. Low, and E. L. Feldman, "Oxidative Stress in the Pathogenesis of Diabetic Neuropathy," *Endocrine Reviews* 25, no. 4 (2004): 612–628, https://doi.org/10.1210/er.2003-0019.

7. S. Bhat, B. Chia, I. P. Barry, A. C. Panayi, and D. P. Orgill, "Free Tissue Transfer in Diabetic Foot Ulcers: A Systematic Review and Meta-Analysis," *European Journal of Vascular and Endovascular Surgery* 66, no. 5 (2023): 670–677, https://doi.org/10.1016/j.ejvs.2023.07.031.

8. J. Su, X. Dong, C. Xu, et al., "ROS-Responsive Hydrogel Enables Drug/Ion/Gas Co-Delivery for Improving Survival of Multi-Territory Perforator Flap in Diabetes," *Advanced Functional Materials* 35, no. 25 (2025): 2500586, https://doi.org/10.1002/adfm.202500586.

9. F. Huang, X. Lu, Y. Yang, et al., "Microenvironment-Based Diabetic Foot Ulcer Nanomedicine," *Advanced Science* 10, no. 2 (2023): 2203308, https://doi.org/10.1002/advs.202203308.

10. E. M. Jones, C. A. Cochrane, and S. L. Percival, "The Effect of pH on the Extracellular Matrix and Biofilms," *Advances in Wound Care* 4, no. 7 (2015): 431–439, https://doi.org/10.1089/wound.2014.0538.

11. J. Tang, W. Liu, Z. Zhang, et al., "ROS-targeting Heterojunction-Integrated GelMA Microneedles for Photo-Responsive Antioxidative Action and Accelerated Diabetic Wound Healing," *Theranostics* 15, no. 18 (2025): 9987–10006, https://doi.org/10.7150/thno.120879.

12. C. Tu, H. Lu, T. Zhou, et al., "Promoting the Healing of Infected Diabetic Wound by an Anti-Bacterial and Nano-Enzyme-Containing Hydrogel With Inflammation-Suppressing, ROS-Scavenging, Oxygen and Nitric Oxide-Generating Properties," *Biomaterials* 286 (2022): 121597, https://doi.org/10.1016/j.biomaterials.2022.121597.

13. Y. Dong and Z. Wang, "ROS-Scavenging Materials for Skin Wound Healing: Advancements and Applications," *Frontiers in Bioengineering and Biotechnology* 11 (2023): 1304835, https://doi.org/10.3389/fbioe.2023.1304835.

14. M. Xing, S. Chen, M. Zhu, et al., "Nanozyme Hydrogels Remodel Pathological Microenvironment for Temporomandibular Joint Osteoarthritis Therapy via Inhibiting MAPK Signal Pathway," *Bioactive Materials* 60 (2026): 216–242, https://doi.org/10.1016/j.bioactmat.2026.01.031.

15. Q. Yu, Z. Zheng, H. Zhang, et al., "Effects of Reactive Oxygen Species and Antioxidant Strategies on Wound Healing in Diabetes," *Interdisciplinary Medicine* 3, no. 2 (2025): 20240062, https://doi.org/10.1002/INMD.20240062.

16. J. Yang, X. Jin, W. Liu, and W. Wang, "A Programmable Oxygenation Device Facilitates Oxygen Generation and Replenishment to Promote Wound Healing," *Advanced Materials* 35, no. 52 (2023): 2305819, https://doi.org/10.1002/adma.202305819.

17. Z. Tao, L. Liu, M. Wu, et al., "Metformin Promotes Angiogenesis by Enhancing VEGFa Secretion by Adipose-Derived Stem Cells via the Autophagy Pathway," *Regenerative Biomaterials* 10 (2023): rbad043, https://doi.org/10.1093/rb/rbad043.

18. C. Chen, X. Li, Y. Hu, et al., "Electrical Stimulation Promoting the Angiogenesis in Diabetic Rat Perforator Flap Through Attenuating Oxidative Stress-mediated Inflammation and Apoptosis," *PeerJ* 12 (2024): 16856, https://doi.org/10.7717/peerj.16856.

19. P. Li, J. Xu, Q. Shi, et al., "Pulse Capacitive Coupling Electric Field Regulates Cell Migration, Proliferation, Polarization, and Vascularization to Accelerate Wound Healing," *Advances in Wound Care* 12, no. 9 (2023): 498–512, https://doi.org/10.1089/wound.2021.0194.

20. W. Li, Z. Liu, X. Tan, et al., "All-In-One Self-Powered Microneedle Device for Accelerating Infected Diabetic Wound Repair," *Advanced Healthcare Materials* 13, no. 13 (2024): 2304365, https://doi.org/10.1002/adhm.202304365.

21. T.-H. Kim, W.-Y. Jeon, Y. Ji, et al., "Electricity Auto-Generating Skin Patch Promotes Wound Healing Process by Activation of Mechanosensitive Ion Channels," *Biomaterials* 275 (2021): 120948, https://doi.org/10.1016/j.biomaterials.2021.120948.

22. D.-Z. Chen, Q. Tang, X. Li, et al., "Biocompatibility of Magnetic Fe_3O_4 Nanoparticles and Their Cytotoxic Effect on MCF-7 Cells," *International Journal of Nanomedicine* 7 (2012): 4973, https://doi.org/10.2147/ijn.S35140.

23. R. Wang, J. Li, X. Wang, et al., "Personalized Nanovaccines Enhance Lymph Node Accumulation and Reprogram the Tumor Microenvironment for Improved Photodynamic Immunotherapy," *Nano Letters* 24 (2024): 7432–7442, https://doi.org/10.1021/acs.nanolett.4c01678.

24. Y. Liu, G. Dzidotor, T. T. Le, et al., "Exercise-Induced Piezoelectric Stimulation for Cartilage Regeneration in Rabbits," *Science Translational Medicine* 14, no. 627 (2022): abi7282, https://doi.org/10.1126/scitranslmed.abi7282.

25. B. Tyler, D. Gullotti, A. Mangraviti, T. Utsuki, and H. Brem, "Polylactic Acid (PLA) Controlled Delivery Carriers for Biomedical Applications," *Advanced Drug Delivery Reviews* 107 (2016): 163–175, https://doi.org/10.1016/j.addr.2016.06.018.

26. E. I. Wisotzki, M. Hennes, C. Schuldt, et al., "Tailoring the Material Properties of Gelatin Hydrogels by High Energy Electron Irradiation," *Journal of Materials Chemistry B* 2, no. 27 (2014): 4297–4309, https://doi.org/10.1039/c4tb00429a.

27. X. Wang, K. Sun, C. Wang, et al., "Ultrasound-Responsive Microfibers Promoted Infected Wound Healing With Neuro-Vascularization by Segmented Sonodynamic Therapy and Electrical Stimulation," *Biomaterials* 313 (2025): 122803, https://doi.org/10.1016/j.biomaterials.2024.122803.

28. Y. Zhao, Y. Cai, W. Wang, et al., "Periosteum-Bone Inspired Hierarchical Scaffold With Endogenous Piezoelectricity for Neuro-Vascularized Bone Regeneration," *Bioactive Materials* 44 (2025): 339–353, https://doi.org/10.1016/j.bioactmat.2024.10.020.

29. R. Luo, Y. Xiong, J. Li, et al., "Piezoelectric Injectable Anti-Adhesive Hydrogel to Promote Endogenous Healing of Tendon Injuries," *Advanced Materials* 37, no. 40 (2025): 2501306, https://doi.org/10.1002/adma.202501306.

30. Y. Xiong, R. Luo, Y. Qi, et al., "Flexible Stretchable Piezoelectric Films for Tissue Repair and Health Detection," *Small Methods* 9, no. 9 (2025): 00247, https://doi.org/10.1002/smtd.202500247.

31. T. Vinikoor, G. K. Dzidotor, T. T. Le, et al., "Injectable and Biodegradable Piezoelectric Hydrogel for Osteoarthritis Treatment," *Nature Communications* 14, no. 1 (2023): 6257, https://doi.org/10.1038/s41467-023-41594-y.

32. W. F. Beyer Jr. and I. Fridovich, "Catalases–With and Without Heme," *Basic Life Sciences* 49 (1988): 651–661.

33. Z. Chen, J. J. Yin, Y. T. Zhou, et al., "Dual Enzyme-Like Activities of Iron Oxide Nanoparticles and Their Implication for Diminishing Cytotoxicity," *American Chemical Society Nano* 6, no. 5 (2012): 4001–4012, https://doi.org/10.1021/nn300291r.

34. A. Aliyev, A. Israyilova, U. Hasanova, Z. Gakhramanova, and A. Ahmadova, "Nanotechnology in Wound Healing: A New Frontier in Regenerative Medicine," *Micro* 5, no. 4 (2025): 60.

35. K. Zhu, R. Li, S. Yin, et al., "A Novel Ultrasound-Driven Piezoelectric GBR Membrane Dispersed With Boron Nitride Nanotubes Promotes Bone Regeneration and Anti-Bacterial Properties," *Materials Today Bio* 30 (2025): 101418, https://doi.org/10.1016/j.mtbio.2024.101418.

36. D. Shan, Y. Shi, S. Duan, Y. Wei, Q. Cai, and X. Yang, "Electrospun Magnetic Poly(l-lactide) (PLLA) Nanofibers by Incorporating PLLA-stabilized Fe_3O_4 Nanoparticles," *Materials Science and Engineering: C* 33, no. 6 (2013): 3498–3505, https://doi.org/10.1016/j.msec.2013.04.040.

37. I. S. Babichuk, C. Lin, Y. Qiu, et al., "Raman Mapping of Piezoelectric Poly(l-Lactic Acid) Films for Force Sensors," *RSC Advances* 12, no. 43 (2022): 27687–27697, https://doi.org/10.1039/d2ra04241j.

38. A. A. La Mattina, S. Mariani, and G. Barillaro, "Bioresorbable Materials on the Rise: From Electronic Components and Physical Sensors to in Vivo Monitoring Systems," *Advanced Science* 7, no. 4 (2020): 1902872, https://doi.org/10.1002/advs.201902872.

39. X. Yu, L. Wang, Z. Zhu, et al., "Piezoelectric Effect Modulates Nanozyme Activity: Underlying Mechanism and Practical Application," *Small* 19, no. 52 (2023): 2304818, https://doi.org/10.1002/smll.202304818.

40. C. Peng, W. Wu, H. Huo, J. Li, and E. Wang, "Defect-Boosted Piezoelectric and Nanozymatic Synergetic Catalysis for Deep Bacterial Abscess Therapy," *American Chemical Society Nano* 19, no. 23 (2025): 21830–21843, https://doi.org/10.1021/acsnano.5c05806.

41. K. Ma, G. Qi, B. Wang, et al., "Ultrasound-Activated Au/ZnO-Based Trojan Nanogenerators for Combined Targeted Electro-Stimulation and Enhanced Catalytic Therapy of Tumor," *Nano Energy* 87 (2021): 106208, https://doi.org/10.1016/j.nanoen.2021.106208.

42. H. Chu, Y. Zhang, Y. Yang, et al., "Flurbiprofen Microneedle Patches for the Management of Acute Postoperative Pain," *Nano Research* 17, no. 8 (2024): 7493–7503, https://doi.org/10.1007/s12274-024-6751-x.

43. X. Mao, R. Cheng, H. Zhang, et al., "Self-Healing and Injectable Hydrogel for Matching Skin Flap Regeneration," *Advanced Science* 6, no. 3 (2019): 1801555, https://doi.org/10.1002/advs.201801555.

44. K. Deng, R. Luo, Y. Chen, et al., "Electrical Stimulation Therapy—Dedicated to the Perfect Plastic Repair," *Advanced Science* 12, no. 24 (2025): 2409884, https://doi.org/10.1002/advs.202409884.

45. X. Wan, W. Wang, and Z. Liang, "Epigallocatechin-3-Gallate Inhibits the Growth of Three-Dimensional In Vitro Models of Neuroblastoma Cell SH-SY5Y," *Molecular and Cellular Biochemistry* 476 (2021): 3141–3148, https://doi.org/10.1007/s11010-021-04154-w.

46. X. Wu, T. Wang, J. Zhao, et al., "Ultrasound-Responsive Piezoelectric Membrane Promotes Osteoporotic Bone Regeneration via the "Two-Way Regulation" Bone Homeostasis Strategy," *Advanced Science* 12, no. 27 (2025): 2504293, https://doi.org/10.1002/advs.202504293.

47. W. Han, Z. Liu, H. Yu, et al., "An Artificial Piezoelectric-Conductive Integrated Peri-Implant Gingiva Enables Efficient Bacterial Inhibition and Soft-Tissue Integration," *Advanced Fiber Materials* 7, no. 4 (2025): 1128–1147, https://doi.org/10.1007/s42765-025-00543-8.

48. R. Montesano and L. Orci, "Tumor-Promoting Phorbol Esters Induce Angiogenesis In Vitro," *Cell* 42, no. 2 (1985): 469–477, https://doi.org/10.1016/0092-8674(85)90104-7.

49. W. Fernando, E. MacLean, S. Monro, et al., "Phloridzin Docosahexaenoate, an Omega-3 Fatty Acid Ester of a Flavonoid Precursor, Inhibits Angiogenesis by Suppressing Endothelial Cell Proliferation, Migration, and Differentiation," *Biomolecules* 14, no. 7 (2024): 769, https://doi.org/10.3390/biom14070769.

50. Z. Zhang, X. Chen, S. Gao, X. Fang, and S. Ren, "3D Bioprinted Tumor Model: A Prompt and Convenient Platform for Overcoming Immunotherapy Resistance by Recapitulating the Tumor Microenvironment," *Cellular Oncology* 47, no. 4 (2024): 1113–1126, https://doi.org/10.1007/s13402-024-00935-9.

51. A. M. Ali and H. Kunugi, "Apitherapy for Age-Related Skeletal Muscle Dysfunction (Sarcopenia): A Review on the Effects of Royal Jelly, Propolis, and Bee Pollen," *Foods* 2020, 9 (10), 1362, https://doi.org/10.3390/foods9101362.

52. Z. Luo, R. Wan, J. Qiu, et al., "Multi-Omics Profiling of a Self-Assembling Bioactive Hydrogel for Immunomodulation and Myogenesis in Volumetric Muscle Loss," *Chemistry* 11, no. 8 (2025): 102645, https://doi.org/10.1016/j.chempr.2025.102645.

53. H. Pouri, R. Panta, P. Bharathan, J. Fang, and J. Zhang, "Advances in Nanostructured Fluorescence Sensors for H_2O_2 Detection: Current Status and Future Direction," *Micro* 5, no. 2 (2025): 15.

54. Y. Chen, Q. Zhang, Y. Wu, C. D. Branch-Brooks, and C. E. Butler, "Short-term Influences of Radiation on Musculofascial Healing in a Laparotomy Rat Model," *Scientific Reports* 9, no. 1 (2019): 11896, https://doi.org/10.1038/s41598-019-48201-5.

55. P. Pelissier, M. Santoul, V. Pinsolle, V. Casoli, and F. Behan, "The Keystone Design Perforator Island Flap. Part I: Anatomic Study," *Journal of Plastic, Reconstructive & Aesthetic Surgery* 60, no. 8 (2007): 883–887, https://doi.org/10.1016/j.bjps.2007.01.072.

56. D. Liu, L. Li, B.-L. Shi, et al., "Ultrasound-Triggered Piezocatalytic Composite Hydrogels for Promoting Bacterial-Infected Wound Healing," *Bioactive Materials* 24 (2023): 96–111, https://doi.org/10.1016/j.bioactmat.2022.11.023.

57. H. Zhang, Z. Wang, Y. Zhu, et al., "ROS-Responsive Double-Layer Microneedles Enable Sequential Antibacterial and Immunomodulatory Therapy for Infected Wound Healing," *Theranostics* 16, no. 4 (2026): 2052–2079, https://doi.org/10.7150/thno.122865.

58. D. A. Mogilenko, J. T. Haas, L. L'homme, et al., "Metabolic and Innate Immune Cues Merge Into a Specific Inflammatory Response via the UPR," *Cell* 177, no. 5 (2019): 1201–1216.e19, https://doi.org/10.1016/j.cell.2019.03.018.

59. S. A. Syed Mortadza, L. Wang, D. Li, and L. H. Jiang, "TRPM2 Channel-Mediated ROS-Sensitive Ca^{2+} Signaling Mechanisms in Immune Cells," *Frontiers in Immunology* 6 (2015): 407, https://doi.org/10.3389/fimmu.2015.00407.

60. Y. Lv, C. Chen, M. Han, et al., "CXCL2: A Key Player in the Tumor Microenvironment and Inflammatory Diseases," *Cancer Cell International* 25, no. 1 (2025): 133, https://doi.org/10.1186/s12935-025-03765-3.

61. A. Korta, J. Kula, and K. Gomułka, "The Role of IL-23 in the Pathogenesis and Therapy of Inflammatory Bowel Disease," *International Journal of Molecular Sciences* 24, no. 12 (2023): 10172, https://doi.org/10.3390/ijms241210172.

Supporting Information

Additional supporting information can be found online in the Supporting Information section.

Supporting File: smll73712-sup-0001-SuppMat.doc.